Reduced volume and reflection for optical tweezers with radial Laguerre-Gauss beams

J.-B. Béguin,[1] J. Laurat,[2] X. Luan,[1] A. P. Burgers,[1,*] Z. Qin,[1,3] and H. J. Kimble[1,†]

[1] *Norman Bridge Laboratory of Physics, California Institute of Technology, Pasadena, California 91125, USA*
[2] *Laboratoire Kastler Brossel, Sorbonne Université, CNRS, ENS-Université PSL, Collège de France, 4 Place Jussieu, 75005 Paris, France*
[3] *State Key Laboratory of Quantum Optics and Quantum Optics Devices, Institute of Opto-Electronics, Shanxi University, Taiyuan 030006, China*

(Dated: February 12, 2020)

Spatially structured light has opened a wide range of opportunities for enhanced imaging as well as optical manipulation and particle confinement. Here, we show that phase-coherent illumination with superpositions of radial Laguerre-Gauss (LG) beams provides improved localization for bright optical tweezer traps, with narrowed radial and axial intensity distributions. Further, the Gouy phase shifts for sums of tightly focused radial LG fields extend the range of imaging methods and permit novel phase-contrast microscopy strategies at the wavelength scale. One application is the suppression of interference fringes from reflection near nano-dielectric surfaces, with the promise of improved cold-atom delivery and manipulation.

Structuring of light has provided advanced capabilities in a variety of research fields and technologies, ranging from microscopy to particle manipulation [1–4]. Coherent control of the amplitude, phase, and polarization degrees of freedom for light enables the creation of engineered intensity patterns and tailored optical forces. In this context, Laguerre-Gauss (LG) beams have been extensively studied. Among other realizations, tight focusing with subwavelength features was obtained with radially polarized beams [5, 6], as well as with opposite orbital angular momentum for copropagating fields [7]. LG beams have also attracted interest for designing novel optical tweezers [8–10]. Following the initial demonstration of a LG-based trap for neutral atoms [11], various configurations have been explored, including 3D geometries with "dark" internal volumes [12–14] for atom trapping with blue-detuned light [15, 16].

For these and other applications of structured light, high spatial resolution is of paramount importance. However in most schemes, resolution transverse to the optic axis exceeds that along the optic axis. For example, an optical tweezer formed from a Gaussian beam with wavelength $\lambda = 1\,\mu\text{m}$ focused in vacuum to waist $w_0 = 1\,\mu\text{m}$ has transverse confinement w_0 roughly $3\times$ smaller than its longitudinal confinement set by the Rayleigh range $z_R = \pi w_0^2/\lambda$. One way to obtain enhanced axial resolution is known as 4π microscopy [17, 18], for which counterpropagating beams form a standing wave with axial spatial scale of $\lambda/2$ over the range of z_R. However, 4π microscopy requires interferometric stability and delicate mode matching. Another method relies on copropagating beams each with distinct Gouy phases [19–21], which was proposed and realized mostly in the context of dark optical traps, either with two Gaussian beams of different waists or offset foci [22, 23], or with two LG modes of different orders [14]. However, for bright trap configurations, a comparable strategy has remained elusive.

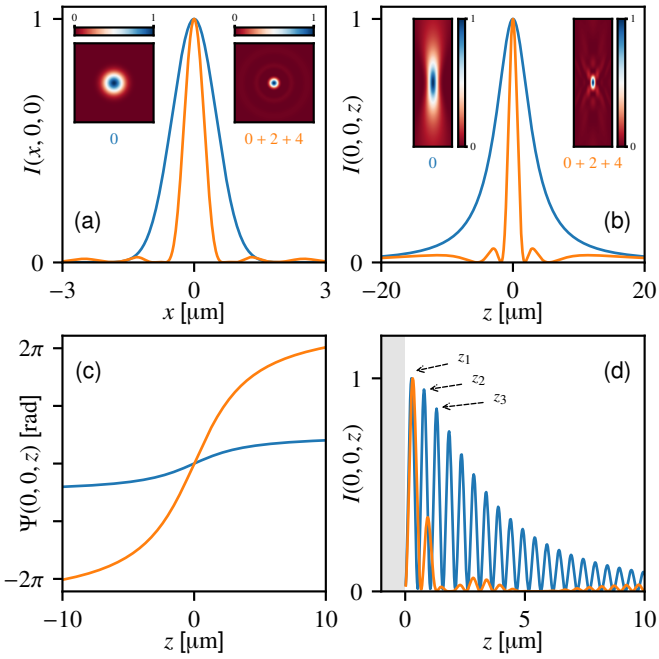

FIG. 1. Comparison between the fundamental Gaussian mode $\vec{E}_0$ (blue) and the superposition of radial p modes $\vec{E}_\Sigma$ (orange) with $p = 0, 2, 4$. The plots are calculated for the paraxial case, with $w_0 = 1\,\mu\text{m}$ and $\lambda = 1\,\mu\text{m}$. (a) x-line cut transverse intensity profiles. Insets provide the x-y distribution in the focal plane. (b) z-line cut axial intensity profiles. Insets correspond to the x-z distribution in the $y = 0$ plane. (c) Gouy phases Ψ_0 (blue) for $\vec{E}_0$ and Ψ_Σ (orange) for $\vec{E}_\Sigma$ along the optical axis z. (d) Reflection fringes due to a semi-infinite planar surface (grey), with amplitude reflection coefficient $r = -0.8$ and focus at the surface $z = 0$. z_i indicate successive maxima. All intensities are normalized to their peak values in (a,b,d).

In this Letter, we show that superpositions of purely radial LG modes can lead to reduced volume for bright optical traps. We also provide a scheme for implemen-

* Present address: Department of Electrical Engineering, Princeton University, Princeton, New Jersey 08540, USA
† hjkimble@caltech.edu

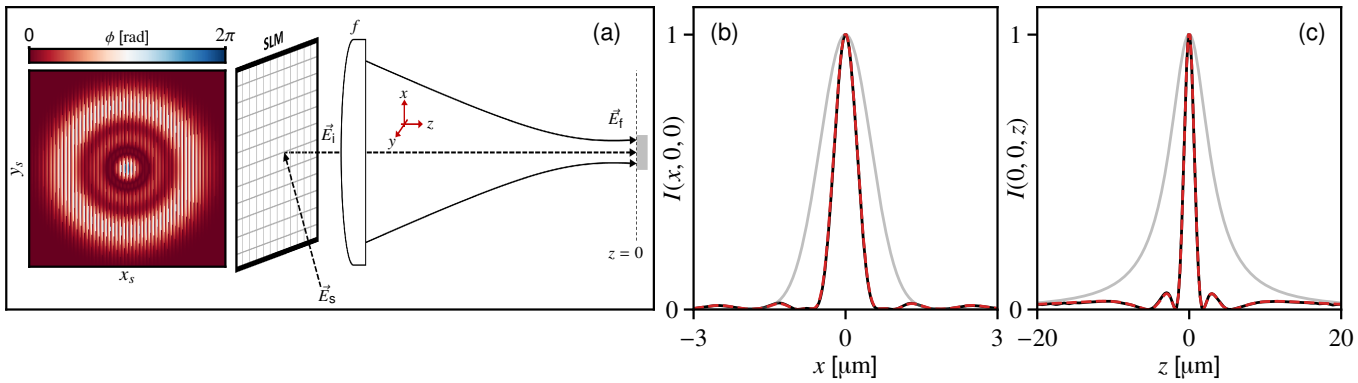

FIG. 2. (a) *left-* Calculated transverse phase profile ϕ applied to the spatial phase modulator (SLM) to generate the field $\vec{E}_\Sigma$. *right-* An incident Gaussian source field $\vec{E}_s$ is incident on the SLM. The first order diffracted field $\vec{E}_i$ on the exit plane of the SLM is then focused by an objective lens with effective focal length f to form the field $\vec{E}_f$ in the focal plane at $z = 0$. (b) Line cuts along x of $|\vec{E}_f|^2$ in the focal plane for modulation of the SLM with $\phi(x_s, y_s)$ calculated to generate $\vec{E}_\Sigma$ (red solid line), ideal target intensity $|\vec{E}_\Sigma|^2$ (black dashed line), and Gaussian intensity $|\vec{E}_0|^2$ (gray line). (c) As in (b), but for line cuts along z with $x = y = 0$.

tation by way of a spatial light modulator (SLM) for beam shaping extended beyond the paraxial approximation into a regime of wavelength-scale traps. Significantly, apart from reduced trap volume, our study highlights differential Gouy phase shifts at the wavelength scale as a novel tool for imaging. An application is the strong suppression of interference fringes from reflections of optical tweezers near surfaces of nanophotonic structures, thereby providing a tool to integrate cold-atom transport and nanoscale quantum optics.

Within the paraxial approximation, we denote the positive frequency component of the electric field by $\vec{E}_{p,i} = \vec{x} u_p(x, y, z; w_i) e^{-ikz}$ with x-oriented linear polarization and propagation directed towards negative z values with longitudinal wave-vector $k > 0$. The cylindrically-symmetric complex scalar amplitude u_p for LG beams is as in [24, 25], and given explicitly in [26]. The parameter w_i denotes the waist, i.e., $1/e^2$ Gaussian beam intensity radius for the fundamental Gaussian beam with $p = 0$. The azimuthal mode number l is dropped with $l = 0$ throughout (i.e., pure radial LG beams with radial number p). For a given optical frequency, the phase of the field relative to that of a plane wave propagating along $-z$ (i.e., the Gouy phase [19–21]) is given by $\Psi_p(z) = \arg(\vec{E}_{p,i} \cdot \vec{x} e^{ikz}) = (2p + 1) \arctan(z/z_{R,i})$, with the Rayleigh range $z_{R,i} = \pi w_i^2/\lambda$.

Although we have analyzed diverse superpositions of radial LG modes, for clarity we confine our discussion here to the particular superposition $\vec{E}_\Sigma = \vec{E}_0 + \vec{E}_2 + \vec{E}_4$. Figure 1(a, b) provide the calculated intensity distributions for the fundamental Gaussian mode $\vec{E}_0$ (blue) and for the superposition (orange), along the x-axis in the focal plane and along the z-propagation axis, respectively. As shown by the line cuts and insets in Figure 1 (a, b), there is a large reduction in focal volume V_Σ for $|\vec{E}_\Sigma|^2$ relative to V_0 for $|\vec{E}_0|^2$. Here, $V = \Delta x \Delta y \Delta z$, with $\Delta x, \Delta y, \Delta z$ taken to be the full widths at half maxima for the intensity distributions along x, y, z in Figure 1(a, b), leading to $V_0/V_\Sigma \simeq 22$ where $V_0 = 8.6\,\mu\text{m}^3$ and $V_\Sigma = 0.39\,\mu\text{m}^3$ as detailed in [26]. Recall that individual u_p modes have identical spatial profiles $|u_p(0, 0, z)|$ along z. The reduced spatial scale for the superposition $\vec{E}_\Sigma$ results from the set of phases $\{\Psi_p(z)\}$ for $p = 0, 2, 4$, with Gouy phases for the total fields $\vec{E}_0$ and $\vec{E}_\Sigma$ shown in Figure 1(c). The Gouy phase for $\vec{E}_\Sigma$ also leads to suppressed interference fringes in regions near dielectric boundaries as shown in Figure 1(d).

A second metric for confinement in an optical tweezer is the frequency of oscillation for atoms trapped in the tweezer's optical potential. The set of trap frequencies for Cs atoms localized within tweezers formed from $\vec{E}_0$ and $\vec{E}_\Sigma$ as in Figure 1(a,b) are presented in [26]. As expected the trap frequencies have significant increases for $\vec{E}_\Sigma$ as compared to $\vec{E}_0$.

Various methods have been investigated to produce LG beams with high purity [27]. A relatively simple technique consists of spatial phase modulation of a readily available Gaussian source beam with a series of concentric circular binary phase steps to replicate the phase distribution of the targeted field $\vec{E}_{p_{target}}$ with $p_{target} > 0$ [28]. The maximum purity for this technique is ~ 0.8, with the deficit of ~ 0.2 due to the creation of p components other than the single p_{target}. Moreover, it is desirable to generate not only high purity LG beams for a single p_{target} but also arbitrary coherent sums of such modes, as for $\vec{E}_\Sigma$. Rather than generate separately each component from the set of required radial modes $\{p\}_{target}$, here we propose a technique with a single SLM that eliminates the need to coherently combine multiple beams for the set $\{p\}_{target}$. Our strategy reproduces simultaneously both the phase and the amplitude spatial distributions of the desired complex electric field (and in principle, the polarization distribution for propagation phenomena beyond the scalar field approximation).

Figure 2(a) illustrates our technique for the case of the target field $\vec{E}_\Sigma$. Amplitude information for the sum of complex fields comprising $\vec{E}_\Sigma$ is encoded in a phase mask by contouring the phase-modulation depth of a superimposed blazed grating as developed in [29, 30]. For atom trapping applications with scalar polarizability, the tweezer trap depth is proportional to the peak optical intensity in the focal plane, where for the coherent field superposition $\vec{E}_\Sigma$, the peak intensity reaches a value identical to that for $\vec{E}_0$ at only 1/9 of the invested trap light power, which helps to mitigate losses associated with the blazed grating.

Figure 2 shows numerical results for a Gaussian source field $\vec{E}_\mathrm{s}$ input to a SLM to create the field $\vec{E}_\mathrm{i}$ leaving the SLM. $\vec{E}_\mathrm{i}$ is then focused by an ideal thin spherical lens and propagated to the focal plane at $z = 0$ by way of the Fresnel-Kirchhoff scalar diffraction integral. The resulting intensity distributions in the focal plane are plotted in Figure 2(b,c) (red solid) for comparison with the ideal $\vec{E}_\mathrm{i} = \vec{E}_0$ (grey solid) and ideal $\vec{E}_\mathrm{i} = \vec{E}_\Sigma$ (black dashed). These results are encouraging for our efforts to experimentally generate tightly focused radial LG superpositions.

Figures 1 and 2 provide a readily accessible understanding of focused LG mode superpositions within the paraxial approximation. To obtain a more accurate description for tight focusing on a wavelength scale, we next consider a vector theory. Using the vectorial Debye approximation [31, 32] and an input field $\vec{E}_0$ with waist $w_0 \gg \lambda$ and polarization aligned along the x-axis, we calculate the field distribution at the output of an aplanatic objective with numerical aperture of NA = 0.7. The filling factor F_0 for the objective with pupil radius R_p is defined as $F_0 = w_0/R_p$, with $F_0 = 0.35$ for the plots in Figure 3. These parameters provide a 1.3 µm waist in the focal plane for the input $\vec{E}_0$. The corresponding intensity distributions along the x-axis in the focal plane and along the propagation axis z are presented in Figure 3 (a), (b), respectively, and are quite similar to those in Figure 1. Reductions in both transverse and longitudinal widths for input $\vec{E}_\Sigma$ relative to $\vec{E}_0$ are evident even in the vector theory with wavelength-scale focusing. Results for tweezer volume and oscillation frequency are detailed in [26] for Figure 3(a), (b), for which $V_0/V_\Sigma \simeq 14$ where $V_0 = 24\,\mu\mathrm{m}^3$ and $V_\Sigma = 1.7\,\mu\mathrm{m}^3$.

Tight focusing is accompanied by a longitudinal polarization component, which leads to a spatially-dependent elliptical polarization and to dephasing mechanisms for atom trapping [33, 34]. Given the local polarization vector $\vec{\epsilon}$, one can define the vector $\vec{C} = \mathrm{Im}(\vec{\epsilon} \times \vec{\epsilon^\star})$, which measures the direction and degree of ellipticity. $|C| = 0$ corresponds to linear polarization while $|C| = 1$ for circular polarization. Figure 3 (c) provides C_y in the focal plane for the superposition input $\vec{E}_\Sigma$. Due to tighter confinement, the polarization gradient reaches $dC_y/dx = 1.6/\mu m$ for input $\vec{E}_\Sigma$, to be compared to $0.4/\mu m$ for $\vec{E}_0$. Fig. 3(d) plots the total field (input plus reflected) for an infinite planar surface in this condition of tight focusing.

Excepting panels (d) in Figures 1 and 3, we have thus far directed attention to free-space optical tweezers for atoms and molecules. However, there are important settings for both particle trapping and imaging in which the focal region is not homogeneous but instead contains significant spatial variations of the dielectric constant over a wide range of length scales from nanometers to microns. Important examples in AMO Physics include recent efforts to trap atoms near nano-photonic structures such as dielectric optical cavities and photonic crystal waveguides (PCWs) [34–40]. These efforts have been hampered by large modification of the trapping potential of an optical tweezer in the vicinity of a nano-photonic structure, principally associated with specular reflection that produces high-contrast interference fringes extending well beyond the volume of the tweezer.

Panels (d) in Figures 1 and 3 investigate a strategy to mitigate this situation by exploiting the rapid spatial variation of the Gouy phase Ψ_Σ for the field $\vec{E}_\Sigma$ as compared to Ψ_0 for the field $\vec{E}_0$. As shown in panels (d), the

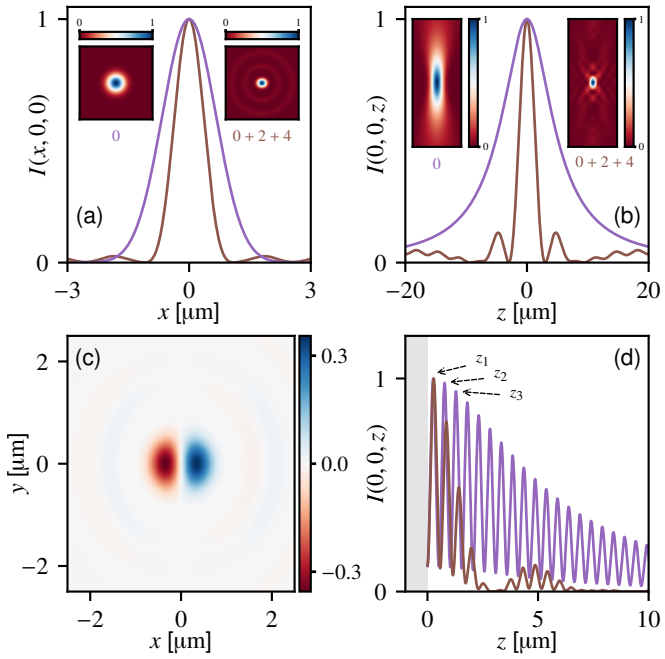

FIG. 3. Focused intensity distributions calculated within the vectorial Debye approximation for inputs $\vec{E}_0$ (violet) and $\vec{E}_\Sigma$ (brown). The numerical aperture is NA = 0.7 with filling factor $F_0 = 0.35$, leading to a focused waist $w_0 \simeq 1.3\,\mu\mathrm{m}$ for input $\vec{E}_0$. (a) x-line cut transverse intensity profiles. The insets provide the x-y intensity distribution in the focal plane $z = 0$. (b) z-line cut axial intensity profiles. The insets correspond to the x-z distribution. (c) Polarization ellipticity C_y in the focal plane for input $\vec{E}_\Sigma$. (d) Reflection fringes from a semi-infinite planar surface, with amplitude reflection coefficient $r = -0.8$. All intensities are normalized to their maximum values in (a,b,d).

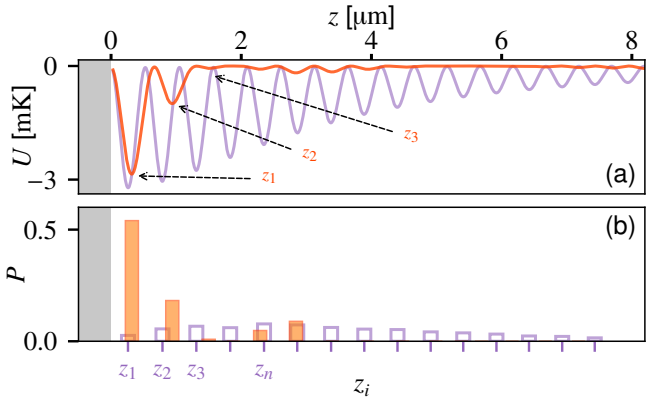

FIG. 4. Results from Monte Carlo simulation of cold atom delivery close to a semi-infinite planar surface with an amplitude reflection coefficient $r = -0.8$. (a) Optical potentials $U(0, 0, z)$ for optical tweezers formed from the fields $\vec{E}_0$ (violet) and $\vec{E}_\Sigma$ (red), respectively, as in Fig. 1(d) for focus at $z = 0$. (b) The final probabilities $P(z_i)$ for delivery of atoms to optical traps centered at positions z_i. Atoms are initially loaded into an optical tweezer of depth $U_0 = 1\,\mathrm{mK}$ at focal distance $z_{initial} = 600\,\mu\mathrm{m}$ from the surface and initial temperature of $100\,\mu\mathrm{K}$. The focal plane of the optical tweezer is then scanned from $z_{initial}$ to $z_{final} = 0\,\mu\mathrm{m}$. Full numerical simulations of atom transport can be found in [26], and provide the basis for this figure.

contrast and spatial extent of the near-field interference is greatly reduced for $\vec{E}_\Sigma$ due to rapid spatial dephasing between input and reflected fields from Ψ_Σ.

To verify that atoms can indeed be efficiently delivered to reflective traps near dielectric surfaces, we performed Monte Carlo simulations of atom trajectories by moving the tweezer's focus position from far away ($z = 600\,\mu\mathrm{m}$) to the surface ($z = 0\,\mu\mathrm{m}$, as shown in Figure 4(a)) for amplitude reflection coefficient $r = -0.8$. We then extracted probabilities for single atoms being delivered and trapped in near surface traps as shown in Figure 4(b). The specific choice of reflection coefficient $r = -0.8$ ($r = -0.3$) is based on numerical simulations of wavelength-scale tweezer reflection from the nanoscale surface of an Alligator Photonic Crystal Waveguide (APCW) as presented in [37] ([39]) for polarization parallel (perpendicular) to the long axis of the APCW. See [26] for $r = -0.3$.

As shown in Figure 4(b), the trap formed by the superposition $\vec{E}_\Sigma$ (orange histogram) leads to large enhancement in delivery efficiencies into near surface traps (z_1, z_2...) as compared to the very small probability of delivery for the conventional trap formed by $\vec{E}_0$ (violet histogram). The probability of delivering an atom into the z_1 trap with $\vec{E}_\Sigma$ is $P_\Sigma(z_1) \simeq 0.55$ as compared to $P_0(z_1) \simeq 0.03$ with $\vec{E}_0$. Figure 4 is from a one-dimensional model of atom transport (i.e., in the optical potential $U(0, 0, z)$), and hence provides only a qualitative guide. We have also carried out full 3D simulations for the situation of Figure 1, with comparable results (e.g., $P_\Sigma(z_1) \simeq 0.45$) presented in [26].

Moreover, beyond the results shown in Figure 4 and in [26], improvements in delivery efficiency have been found by including atom cooling in the simulations at various stages of the transport, as well as applying blue-detuned guided-mode (GM) beams as atoms arrive near the surface to overcome loss due to surface forces such as the Casimir-Polder potential. More importantly, we stress that our method for atom delivery to nano-photonic devices can be readily extended to 2D slab PCWS [41, 42]. Finally, to document the robustness of our scheme, results from simulations analogous to those in Figure 4 are presented in [26] for $r = -0.3$ corresponding to an optical tweezer with polarization perpendicular to the long axis of an APCW, for which $P_\Sigma(z_1) \simeq 0.68$.

In conclusion, we have shown that coherent superpositions of radial LG beams can lead to tightly focused optical tweezers with reduced volume and increased trapping frequency. A specific application has been presented for the efficient transport of atoms via optical tweezers directly to trap sites near the surface of a reflecting dielectric. We are currently investigating other applications of the rapid variation of the Gouy phase within wavelength-scale focal regions, including phase-contrast microscopy within heterogeneous sample volumes.

FUNDING INFORMATION

ONR Grant No. N000141612399; ONR MURI Quantum Opto-Mechanics with Atoms and Nanostructured Diamond Grant No. N000141512761; AFOSR MURI Photonic Quantum Matter Grant No. FA95501610323; NSF Grant No. PHY1205729; Caltech KNI; French-US Fulbright Commission; French National Research Agency (NanoStrong project ANR-18-CE47-0008); Region Ile-de-France (DIM SIRTEQ).

ACKNOWLEDGMENTS

The authors thank Robert Boyd and Nick Black for discussions related to SLMs.

Appendix A

We give details into our atomic trajectory simulations, as well as the dependence of diffraction on the spatial properties of the focused radial LG beam distributions. Accompanying movies from numerical simulations are also provided.

Appendix A: Field expression

For convenience, the expression for the complex scalar amplitude function is reproduced here from [24, 25]

$$u_p(r,z) \propto \frac{1}{\omega(z)} \exp\left(-\frac{r^2}{\omega(z)^2}\right) \exp\left(-ik\frac{r^2}{2R(z)}\right) \times L_p^0\left(\frac{2r^2}{\omega(z)^2}\right) \exp\left(i\Psi(z)\right) \tag{A1}$$

with ω_0 the waist, $z_R = \pi\omega_0^2/\lambda$ the Rayleigh range, $R(z) = z(1 + z_R^2/z^2)$ the radius of curvature and $\omega(z) = \omega_0\sqrt{1 + z^2/z_R^2}$ the waist at position z. The Gouy phase

is given by $\Psi(z) = (2p+1)\arctan(z/z_R)$ and L_p^0 corresponds to the associated Laguerre polynomial.

Appendix A: Trap frequencies and dimensions in the paraxial limit

One metric for confinement of an atom of mass M in an optical tweezer is the frequency of oscillation near the bottom of the tweezer's optical potential. Relative to the trap formed by $\vec{E}_0$ in Figure 2, radial and axial trap frequencies for $\vec{E}_\Sigma$ are increased as $\omega_r^\Sigma = \omega_r^0\sqrt{5}$ and $\omega_z^\Sigma = \omega_z^0\sqrt{35/3}$, with trap depth U_0 for both $\vec{E}_0$ and $\vec{E}_\Sigma$. For Cs atoms with $U_0 = 1$mK, wavelength $\lambda = 1\,\mu$m, and waist $w_0 = 1\,\mu$m, $\omega_r^\Sigma = 2\pi \times 178\,$kHz and $\omega_z^\Sigma = 2\pi \times 61\,$kHz. Here, $\omega_r^0 = \sqrt{4U_0/Mw^2}$ and $\omega_z^0 = \sqrt{2U_0/Mz_R^2}$ are the radial and axial angular trap frequencies for an ideal Gaussian mode $\vec{E}_0$, with an accuracy better than 1% as compared to the ground state trap frequencies obtained by numerical solution of the spatial Schrödinger equation.

The full widths at half maxima for the intensity distributions along x, y, z in Figure 1 of the main text are $\Delta x^0 = \Delta y^0 = 1.17\,\mu$m and $\Delta z^0 = 6.28\,\mu$m for $\vec{E}_0$, and $\Delta x^\Sigma = \Delta y^\Sigma = 0.51\,\mu$m and $\Delta z^\Sigma = 1.5\,\mu$m for $\vec{E}_\Sigma$.

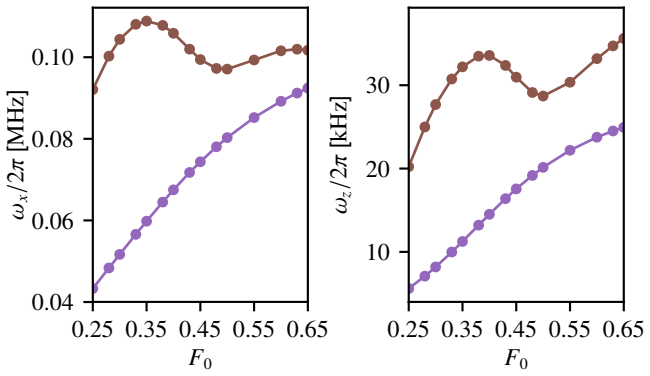

FIG. 5. Dependence of the angular radial (x-cut) (a) and (b) axial trap frequencies (ω_x and ω_z at the bottom of the trap) as functions of the objective lens filling factor F_0, with fixed numerical aperture NA = 0.7. (Violet) the input field distribution is $\vec{E}_0$; (Brown) the input field distribution is $\vec{E}_\Sigma$.

Appendix A: Filling factor dependence, trap frequencies and dimensions

Pupil apodization and diffraction effects modify the spatial properties of the focused radial Laguerre-Gauss beams according to their radial mode number p [43]. As an example, we show in Figure 5 the variation of the trap frequencies at the bottom of the trap for the two light field distributions $\vec{E}_0$ and $\vec{E}_\Sigma$ as a function of the objective lens filling factor F_0 within the vectorial Debye propagation model [31, 32]. The angular trap frequencies ω_x and ω_z are obtained by numerically solving the spatial time-independent Schrödinger's equation for a single Cesium atom and a scalar optical trap potential with depth of 1 mK (for $6S_{1/2}$). We reproduce in the top panels (a) and (b) of Figure 6 the radial and axial intensity profiles for a filling factor $F_0 = 0.35$ as given in Figure 3 of the main text, while the bottom panels (c) and (d) correspond to $F_0 = 0.45$. For the latter, the $1/e^2$ focused intensity radius of $\vec{E}_0$ is 1 µm.

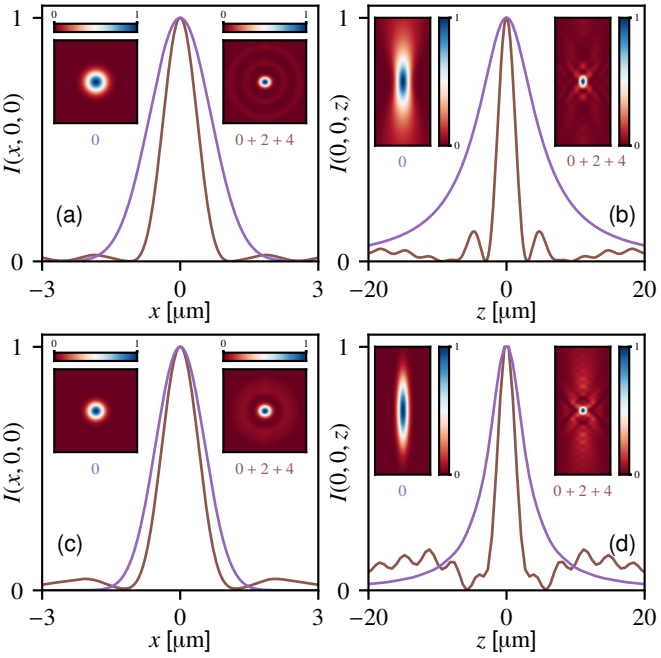

FIG. 6. Focused intensity distributions calculated within the vectorial Debye approximation for inputs $\vec{E}_0$ (violet) and $\vec{E}_\Sigma$ (brown). The numerical aperture is NA = 0.7 and two filling factor values are compared: For $F_0 = 0.35$ (as in main article) (a) x-line cut transverse intensity profiles. The insets provide the x-y intensity distribution in the focal plane $z = 0$. (b) z-line cut axial intensity profiles. The insets correspond to the x-z distribution. For $F_0 = 0.45$ (c,d). Plotted intensities for inputs $\vec{E}_0$ (violet) and $\vec{E}_\Sigma$ (brown) are normalized to their maximum values.

The choice of the local extremum at small value $F_0 \sim 0.35$ not only alleviates practical requirements of the objective lens (e.g., focal length and working distance) but also permits a description of the focused fields not dominated by diffraction losses. Evident in Figure 3 is that reductions in both transverse and longitudinal widths for input $\vec{E}_\Sigma$ relative to $\vec{E}_0$ are present even in the vector theory with wavelength-scale focusing. For the scalar polarizability of Cs, trap frequencies for input $\vec{E}_\Sigma$ are evaluated to be $\omega_x^\Sigma = 2\pi \times 124\,$kHz and $\omega_z^\Sigma = 2\pi \times 33\,$kHz for this configuration. In terms of trap dimensions, the values corresponding to Figure 3 of the main text are $\Delta x^0 = 1.55\,\mu$m, $\Delta y^0 = 1.51\,\mu$m and $\Delta z^0 = 10.3\,\mu$m; and $\Delta x^\Sigma = 0.84\,\mu$m, $\Delta y^\Sigma = 0.72\,\mu$m and $\Delta z^\Sigma = 2.78\,\mu$m.

Appendix A: Atom trajectory simulation

In the Monte Carlo simulation of atom transport from free space tweezers to near surface traps, the atom sample is initialized from a sample of temperature 100 µK in 1 mK trap depth with position $\simeq$ 600 µm away from the surface. The tweezer focus is then accelerated with acceleration $a = 1\,\mathrm{m\,s^{-2}}$ towards the surface for 20 ms and then moves at constant velocity for 10 ms before decelerating with acceleration $a = -1\,\mathrm{m\,s^{-2}}$ to stop at the surface ($z = 0\,\mu\mathrm{m}$) as shown in Fig. 7. To demonstrate the robustness of our scheme, we also simulated the atom transport with reflection coefficient $r = -0.3$. Fig. 8(a) shows the final frame for traps near the surface. As shown in Fig. 8(b), atoms are mostly delivered into the first two traps near the surface (z_1 and z_2). The probability of atom being delivered to z1 trap is 68.4%. Animations of typical atom trajectories are available in the accompanying supplementary files.

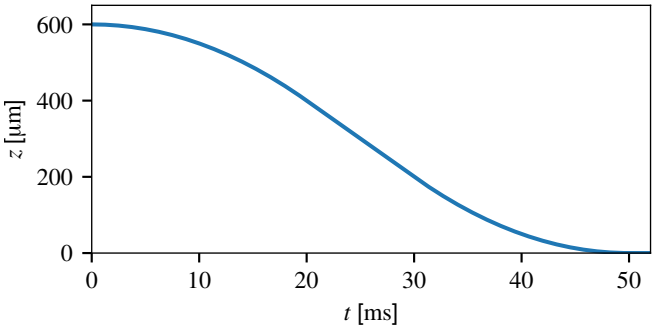

FIG. 7. Motion profile of the focal tweezer position used for the Monte Carlo simulations of fig. 8, 9.

Appendix A: Media for 1D simulation

Here we provide a description of the four movies associated with Figure 9, which are available at *http://dx.doi.org/10.22002/D1.1343*. All movies are generated under the paraxial approximation with $w_0 = 1\,\mu\mathrm{m}$ and normalized to a trap depth of $U/k_B = 1\,\mathrm{mK}$ in absence of the reflecting surface. The black dots represent the individual atoms. The motion profile for the optical tweezer is given in Fig. 7.

Appendix A: Media for 3D simulation

Beyond simulations in 1D, we have also investigated atom transport in 3D for the moving tweezer potential $U(x(t), y(t), z(t))$, as shown in Movie 3D at the following link *http://dx.doi.org/10.22002/D1.1346*. Movie 3D shows the intensity of an $\vec{E}_\Sigma$ tweezer with focus moving towards $z = 0$. The black dots represent individual atoms $\{i\}$ whose trajectories (i.e., positions $x_i(t), y_i(t), z_i(t)$ are driven by forces from $U(x_i(t), y_i(t), z_i(t))$. The parameters are as in Fig. 9, again in the paraxial approximation with $w_0 = 1\,\mu\mathrm{m}$ and normalized to a trap depth of $U/k_B = 1\,\mathrm{mK}$ in absence of the reflecting surface. The

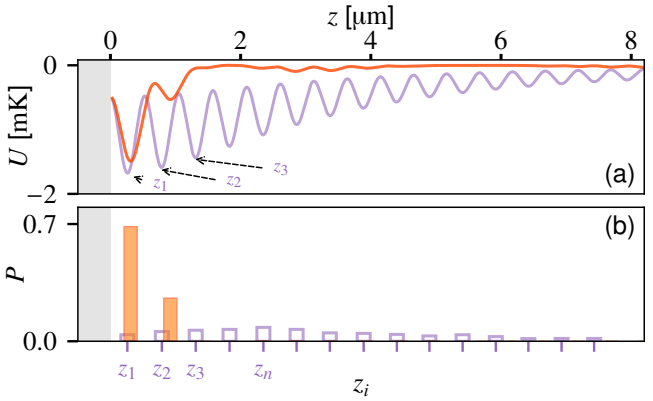

FIG. 8. Results from a Monte Carlo simulation of cold atom delivery close to a semi-infinite planar surface with an amplitude reflection coefficient $r = -0.3$. (a) Optical potentials $U(0, 0, z)$ for optical tweezers formed from the fields $\vec{E}_0$ (violet) and $\vec{E}_\Sigma$ (red), respectively, for focus at $z = 0$. (b) The final probabilities $P(z_i)$ for delivery of atoms to optical traps centered at positions z_i. Atoms are initially loaded into an optical tweezer of depth $U_0 = 1\,\mathrm{mK}$ at focal distance $z_{initial} = 600\,\mu\mathrm{m}$ from the surface and initial temperature of 100 µK. The focal plane of the optical tweezer is then scanned from $z_{initial}$ to $z_{final} = 0\,\mu\mathrm{m}$, as in Fig. 7.

3D results for trajectories are rendered into 2D by an orthographic projection into the x, z plane.

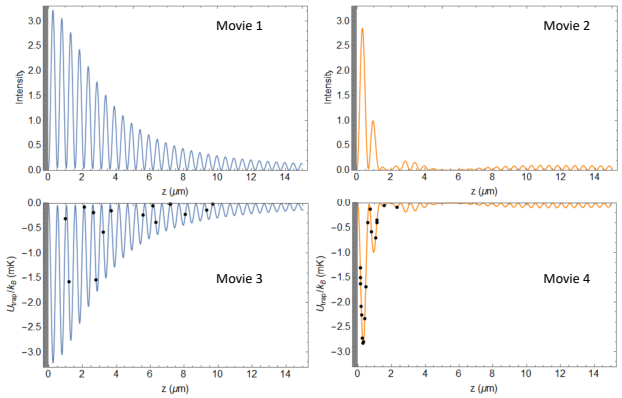

FIG. 9. Last frames of accompanying Movies 1,2,3, and 4, which are available at *http://dx.doi.org/10.22002/D1.1343*. The simulations are carried out in the paraxial approximation as in Figure 1 in the main text with $w_0 = 1\,\mu\mathrm{m}$ and normalized to a trap depth of $U/k_B = 1\,\mathrm{mK}$ in the absence of the reflecting surface at $z = 0$, which has $r = -0.8$. Specifically, Movie 1 represents the intensity of $\vec{E}_0$ tweezer with focus moving towards $z = 0$; Movie 2 represents the intensity of $\vec{E}_\Sigma$ tweezer with focus moving towards $z = 0$; Movie 3 represents atom trajectory simulation for $\vec{E}_0$ tweezer and Movie 4 represents atom trajectory simulation for $\vec{E}_\Sigma$. The black dots represent the individual atoms.

[1] L. Allen, S.M. Barnett, and M.J. Padgett, "Optical Angular Momentum," IOP Publishing (2003).

[2] A. Ashkin, "Optical Trapping and Manipulation of Neutral Particles Using Lasers", World Scientific (2006)

[3] D.G. Grier, "A revolution in optical manipulation," Nature **424**, 810-816 (2003).

[4] Q. Zhan, "Cylindrical vector beams: from mathematical concepts to applications," Adv. Opt. Photonics **1**, 1 (2009).

[5] R. Dorn, S. Quabis, and G. Leuchs, "Sharper focus for a radially polarized light beam," Phys. Rev. Lett. **91**, 233901 (2003).

[6] H. Wang, L. Shi, B. Lukyanchuk, C. Sheppard, and T.C. Chong, "Creation of a needle of longitudinally polarized light in vacuum using binary optics," Nat. Photon. **2**, 501 (2008).

[7] P. Woźniak, P. Banzer, F. Bouchard, E. Karimi, G. Leuchs, and R.W. Boyd, "Tighter spots of light with superposed orbital-angular momentum beams," Phys. Rev. A **94**, 021803(R) (2016).

[8] M. Padgett and R. Bowman, "Tweezers with a twist," Nat. Photon. **5**, 343-348 (2011)

[9] S. Franke-Arnold, "Optica angular momentum and atoms," Phil. Trans. R. Soc. A **375**, 20150435 (2017).

[10] M. Babiker, D. L. Andrews, annd V. E. Lembessis, "Atoms in complex twisted light," J. Opt. **21**, 013001 (2019).

[11] T. Kuga, Y. Torii, N. Shiokawa, T. Hirano, Y. Shimizu, and H. Sasada, "Novel optical trap of atoms with a doughnut beam," Phys. Rev. Lett. **78**, 4713 (1997).

[12] J. L. Chaloupka, Y. Fisher, T. J. Kessler, and D. D. Meyerhofer,"Single-beam, ponderomotive-optical trap for free electrons and neutral atoms," Opt. Lett. **22**, 1021 (1997).

[13] R. Ozeri, L. Khaykovich, and N. Davidson, "Long spin relaxation times in a single-beam blue-detuned optical trap," Phys. Rev. A **59**, R1750 (1999).

[14] J. Arlt and M. Padgett, "Generation of a beam with a dark focus surrounded by regions of higher intensity: the optical bottle beam," Opt. Lett. **25**, 191 (2000).

[15] P. Xu, X. He, J. Wang, and M. Zhan, "Trapping a single atom in a blue detuned optical bottle beam trap," Opt. Lett. **35**, 2164 (2010).

[16] D. Barredo, V. Lienhard, P. Scholl, S. de Léséleuc, T. Boulier, A. Browaeys, and T. Lahaye,"Three-Dimensional Trapping of Individual Rydberg Atoms in Ponderomotive Bottle Beam Traps," Phys. Rev. Lett. **124**, 023201 (2020).

[17] S. Hell and E. H. K. Stelzer, "Properties of a 4Pi confocal fluorescence microscope," J. Opt. Soc. Am. A **9**, 2159 (1992).

[18] N. Bokor and N. Davidson, "Toward a spherical spot distribution with 4π focusing of radially polarized light," Opt. Lett. **29**, 1968 (2004).

[19] R. W. Boyd, "Intuitive explanation of the phase anomaly of focused light beams," J. Opt. Soc. Am. **70**, 877 (1980).

[20] O. Steuernagel, E. Yao, K. O'Holleran, and M. Padgett, "Observation of Gouy-phase-induced transversal intensity changes in focused beams," J. Mod. Opt. **52**, 2713 (2005).

[21] T. Birr, T. Fischer, A. B. Evlyukhin, U. Zywietz, B. N. Chichkov, and C. Reinhardt, "Phase-Resolved Observation of the Gouy Phase Shift of Surface Plasmon Polaritons," ACS Photonics **4**, 905 (2017).

[22] L. Isenhower, W. Williams, A. Dally, and M. Saffman, "Atom trapping in an interferometrically generated bottle beam trap," Opt. Lett. **34**, 1159 (2009).

[23] A. I. Whiting, A. F. Abouraddy, B. E. A. Saleh, M. C. Teich, and J. T. Fourkas, "Polarization-assisted transverse and axial optical superresolution," Opt. Express **11**, 1714 (2003).

[24] L. Allen, M. W. Beijersbergen, R. J. C. Spreeuw, and J. P. Woerdman, "Orbital angular momentum of light and the transformation of Laguerre-Gaussian laser modes," Phys. Rev. A **45**, 8185 (1992).

[25] A.E. Siegman, "Lasers," (Oxford University, Oxford, 1986).

[26] Refer to accompanying Supplemental Material.

[27] T. Ando, Y. Ohtake, Naoya Matsumoto, T. Inoue, N. Fukuchi, "Mode purities of Laguerre-Gaussian beams generated via complex-amplitude modulation using phase-only spatial light modulators," Opt. Lett. **34** (2009)

[28] J. Arlt, K. Dholakia, L.Allen, and M. J. Padgett, "The production of multiringed LaguerreGaussian modes by computer-generated holograms," Journal of Modern Optics **6** 1231 (1998)

[29] J. A. Davis, D. M. Cottrell, J. Campos, M. J. Yzuel and I. Moreno, "Encoding amplitude information onto phase-only filters," Appl. Opt. **23** (1999).

[30] E. Bolduc, N. Bent, E. Santamato, E. Karimi and R. W. Boyd, "Exact solution to simultaneous intensity and phase encryption with a single phase-only hologram," Opt. Lett. **18**, 3546 (2013).

[31] B. Richards and E. Wolf, "Electromagnetic diffraction in optical systems, II. Structure of the image field in an aplanatic system," Proc. R. Soc. A **253**, 358 (1959).

[32] L. Novotny and B. Hecht, "Principles of Nano-Optics," (Cambridge University Press, Cambridge, UK, 2006).

[33] S. Kuhr, W. Alt, D. Schrader, I. Dotsenko, Y. Miroschnychenko, A. Rauschenbeutel, and D. Meschede, "Analysis of dephasing mechanisms in a standing-wave dipole trap," Phys. Rev. A **72**, 023406 (2005).

[34] J.D. Thompson, T.G. Tiecke, A.S. Zibrov, V. Vuletić, and M.D. Lukin, "Coherence and Raman Sideband Cooling of a Single Atom in an Optical Tweezer," Phys. Rev. Lett. **110**, 133001 (2013).

[35] D.E. Chang, J.S. Douglas, A. González-Tudela, C.-L. Hung, and H.J. Kimble, "Colloquium: Quantum matter built from nanoscopic lattices of atoms and photons," Rev. Mod. Phys. **90**, 031002 (2018).

[36] T. Tiecke, J.D. Thompson, N.P. de Leon, L. Liu, V. Vuletić, and M.D. Lukin, "Nanophotonic quantum phase switch with a single atom," Nature **508**, 241-244 (2014).

[37] J.D. Hood, A. Goban, A. Asenjo-Garcia, M. Lu, S.-P. Yu, D. E. Chang, and H. J. Kimble, "Atom-atom interactions around the band edge of a photonic crystal waveguide," Proc. Natl. Acad. Sci. U.S.A. **113**, 10507-10512 (2016).

[38] J.B. Béguin, A.P. Burgers, X. Luan, Z. Qin, S.P. Yu, and H.J. Kimble, "An advanced apparatus for the integration of nanophotonics and cold atoms," Optica **7**, 1 (2020).

[39] A. P. Burgers, L. S. Peng, J. A. Muniz, A. C. McClung, M. J. Martin, and H. J. Kimble, "Clocked atom delivery to a photonic crystal waveguide," Proc. Natl. Acad. Sci. U.S.A. **116**, 456-465 (2019).

[40] M.E. Kim, T.-H. Chang, B.M. Fields, C.-A. Chen, and C.-H. Hung, "Trapping single atoms on a nanophotonic circuit with configurable tweezer lattices," Nat. Commun. **10**, 1647 (2019).

[41] S.-P. Yu, J. A. Muniz, C.-L. Hung, and H. J. Kimble, "Two-dimensional photonic crystals for engineering atomlight interactions," Proc. Natl. Acad. Sci. U.S.A. **116**, 12743-12751 (2019)

[42] A. González-Tudela, C.-L. Hung, D. E. Chang, J. I. Cirac, and H. J. Kimble, "Subwavelength vacuum lattices and atom-atom interactions in two-dimensional photonic crystals," Nat. Photon. **9**, 320-325 (2015).

[43] S. Haddadi, D. Louhibi, A. Hasnaoui, A. Harfouche, and K. Aït-Ameur, "Spatial properties of a diffracted high-order radial LaguerreGauss LG_{p0} beam," Laser Physics, **25**, 125002 (2015).